nature astronomy

SUPPLEMENTARY INFORMATION

https://doi.org/10.1038/s41550-020-1009-3

In the format provided by the authors and unedited.

The water abundance in Jupiter's equatorial zone

Cheng Li[1*], Andrew Ingersoll[1], Scott Bolton[2], Steven Levin[3], Michael Janssen[3], Sushil Atreya[4], Jonathan Lunine[5], Paul Steffes[6], Shannon Brown[3], Tristan Guillot[7], Michael Allison[8], John Arballo[3], Amadeo Bellotti[9], Virgil Adumitroaie[3], Samuel Gulkis[3], Amoree Hodges[6], Liming Li[10], Sidharth Misra[3], Glenn Orton[3], Fabiano Oyafuso[3], Daniel Santos-Costa[2], Hunter Waite[2] and Zhimeng Zhang[1]

[1]California Institute of Technology, Pasadena, CA, USA. [2]Southwest Research Institute, San Antonio, TX, USA. [3]Jet Propulsion Laboratory, California Institute of Technology, Pasadena, CA, USA. [4]University of Michigan, Ann Arbor, MI, USA. [5]Cornell University, Ithaca, NY, USA. [6]Georgia Institute of Technology, Atlanta, GA, USA. [7]Université Côte d'Azur, OCA, Lagrange CNRS, Nice, France. [8]Goddard Institute for Space Studies, New York, NY, USA. [9]Lockheed Martin, Grand Prairie, TX, USA. [10]University of Houston, Houston, TX, USA. *e-mail: cli@gps.caltech.edu

Supplementary Material A: Synthetic Study

While the 0.6 GHz channel observations are consistent among perijoves discussed in the paper and shown in Fig. 1, the error bars on the opacity are too great to confidently constrain the water abundance. Knowledge of the opacity at 0.6 GHz can be improved with further laboratory measurements planned in the future. In this appendix, we illustrate the potential benefit of including the 0.6 GHz channel in our analysis with improved opacity knowledge via a synthetic study. The synthetic spectra of the atmosphere are created by fixing $x\mathrm{NH}_3 = 2.7$ time solar, $\Theta = 132.1$ K, $f_x = 1.2$, $p_D = 2$ bar, and varying the water abundance from 2 to 6 times solar. Then we add ensemble noise (including instrument, calibration, atmospheric variability and deconvolution) to both the nadir brightness temperature and the limb-darkening (see error bars in Fig. 2) to obtain the synthetic spectra, assuming we know the opacity at 0.6 GHz equally as well as the other channels. Finally, we perform a similar inversion as described in the main manuscript using the synthetic spectra with and without the 0.6 GHz channel. Fig. A1 shows the inferred distribution of water with the 0.6 GHz channel and Fig. A2 shows the same inversion without the 0.6 GHz channel. With the 0.6 GHz channel, the lower bound of the water abundance can be much better constrained than that without because a tighter constraint on the ammonia abundance propagates to a tighter constraint for water through the degeneracy between ammonia and water shown in Fig. 6a. It is also worth noting that the distribution of water in the left panel of Fig. A2 (from inverting the synthetic spectra) is almost the same as that in the middle panel of Fig. 5 (from inverting the real spectra), which indicates that our estimation of the error in the water abundance is realistic.

Supplementary Material B: Analysis of best-fit solution

Using the median values of the probability distribution shown in Fig. 5, we compute the nadir brightness temperature and the limb-darkening at 45, 30, and 15 degrees emission angle as a function of frequency (Fig. B1). The observations with error estimates (red crosses) are plotted on top of the modeled spectra. The difference between the model and the deconvolved data is within errors for 1.25 – 22 GHz channels. Note that there is a slight systematic difference (~2%) between perijoves, probably due to spatial and temporal variations in the atmosphere. Because our model does not account for these variabilities, it is not helpful to perform inversions for each perijove. Instead, they are treated as ensemble uncertainties as explained in the main text. For the 0.6 GHz channel, the uncertainty is very large due to the lack of laboratory opacity data at high temperature and pressure. Since we were unable to quantify the errors in opacity at 0.6 GHz, we did not use this channel to derive the water abundance. In order to compare directly with the observations, we convolve the modeled pencil beam brightness temperature with the antenna beam pattern and run it through the orbital trajectory. Fig. B2 shows the residual antenna temperature versus emission angle for the 2.6 GHz channel (most sensitive to water), accumulating all observations from PJ1-PJ9 and between 0 to 4 degrees north. The spread of the dots is mostly due to atmospheric spatial or time variability. The mean residual brightness temperatures are within 2% of the observations and are consistent with the error estimates.

Reference

1. Asplund, M., Grevesse, N., Sauval, A. J. & Scott, P. The Chemical Composition of the Sun. *Annual Review of Astronomy and Astrophysics* **47**, 481–522 (2009).
2. Atreya, S. K. *et al.* The origin and evolution of Saturn, with exoplanet perspective. *Saturn in the 21st Century* **20**, 5–43 (2019).

Table 1. Juno perijove dates, orbit types, System III west longitudes at equator crossing and minimum emission angle of each perijove.

	PJ Dates	Orbital types	Sys III west longitude	Min. emis. angle
PJ1	08/27/2016	Grav	96.6	2.45
PJ3	12/11/2016	Grav	6.8	20.10
PJ4	02/02/2017	MWR	276.5	0.27
PJ5	03/27/2017	MWR-tilt	186.8	0.46
PJ6	05/19/2017	Grav	142.0	15.22
PJ7	07/11/2017	MWR	51.9	0.35
PJ8	09/01/2017	Grav	321.9	24.08
PJ9	10/24/2017	MWR-tilt	231.7	3.89

Table 2. Elemental abundance used in the main article. The solar abundances are calculated from Asplund et al. (2009)[1] and Protosolar abundances are from Atreya et al. (2019)[2]. The protosolar abundances relative to hydrogen are obtained from the present day solar values increased by +0.04 dex, except for He for which the factor is +0.05 dex.

	Solar (Asplund et al., 2009)	Protosolar (Atreya et al., 2019)
He/H	8.51×10^{-2}	9.55×10^{-2}
C/H	2.69×10^{-4}	2.95×10^{-4}
O/H	4.90×10^{-4}	5.37×10^{-4}
N/H	6.76×10^{-5}	7.41×10^{-5}
S/H	1.32×10^{-5}	1.45×10^{-5}
P/H	2.57×10^{-7}	2.82×10^{-7}
Ne/H	8.51×10^{-5}	9.33×10^{-5}
Ar/H	2.51×10^{-6}	2.75×10^{-6}
Kr/H	1.78×10^{-9}	1.95×10^{-9}
Xe/H	1.74×10^{-10}	1.91×10^{-10}

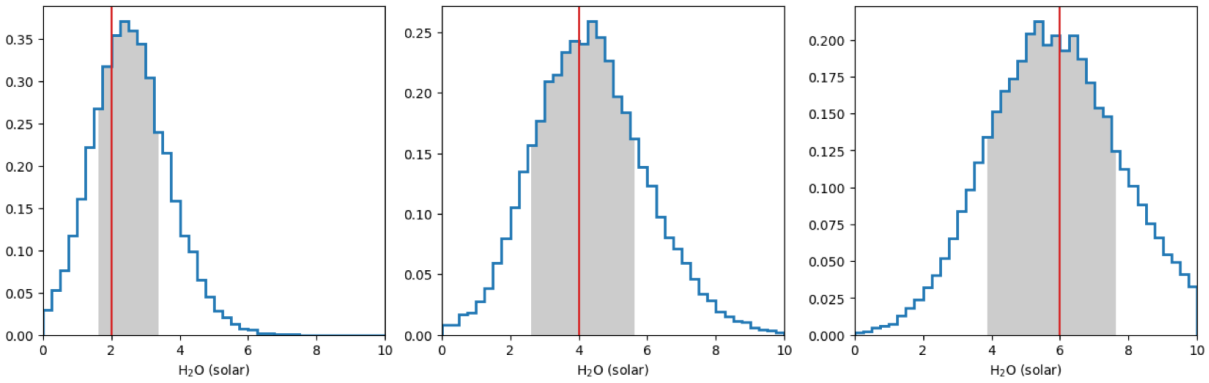

Figure A1: Inferred distribution of deep water abundance based on 0.6 – 22 GHz channels using synthetic spectra. The true water abundances were varied from 2, to 4, to 6 times solar, indicated by the red lines. Y-axis is the probability density.

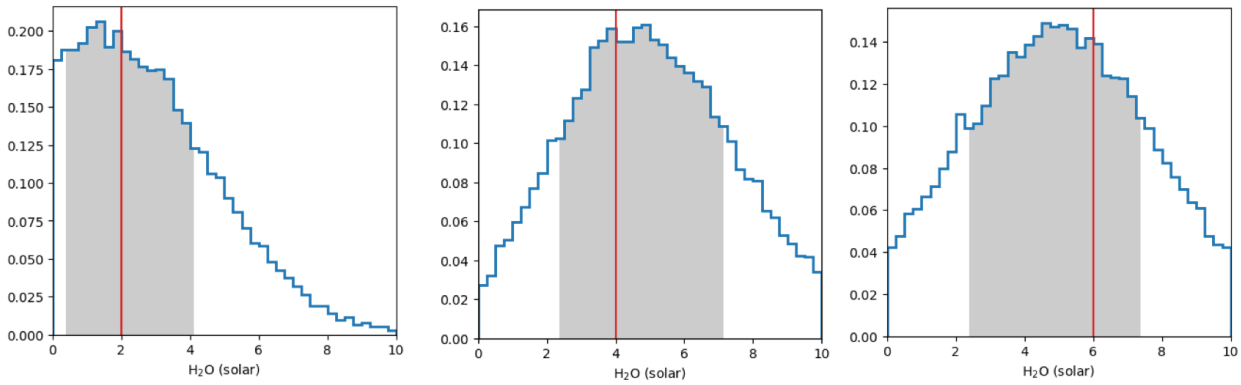

Figure A2: Similar to Figure A1 but based on 1.25 – 22 GHz channels.

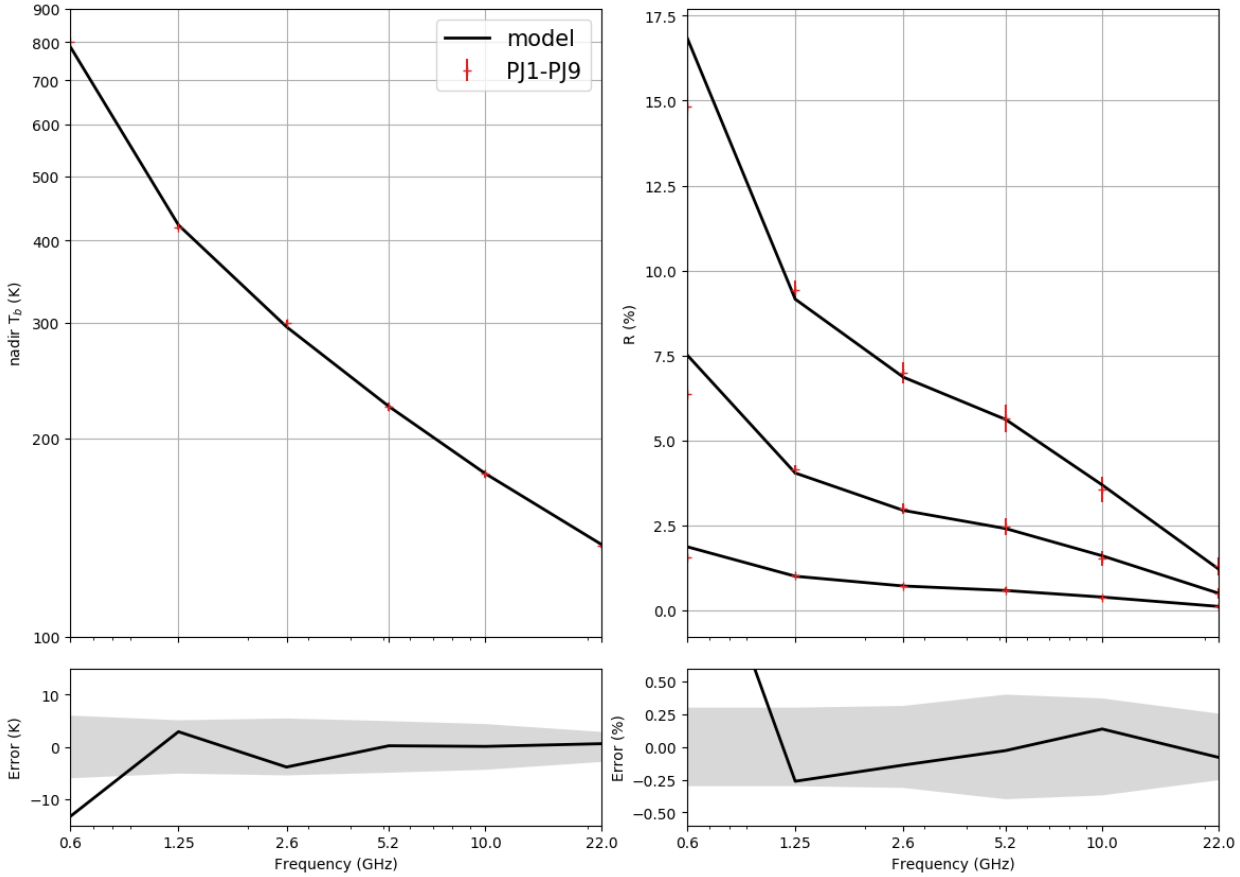

Figure B1. Nadir brightness temperature (left) and limb-darkening (right) spectra. Ensemble measurements of PJ1 – PJ9 between 0 – 5 degrees are plotted in red. Black lines show the best-fit model. The three curves in the right panel represent limb-darkening at 45°, 30° and 15° ordered from top to bottom. The bottom two panels show the error between the best-fit model and the measurements. 1σ confidence interval of the measurements is shaded. The radiometric bandwidths of each channel from 0.6 GHz to 22 GHz are 0.021 GHz, 0.044 GHz, 0.084 GHz, 0.17 GHz, 0.33 GHz, 0.77 GHz respectively.

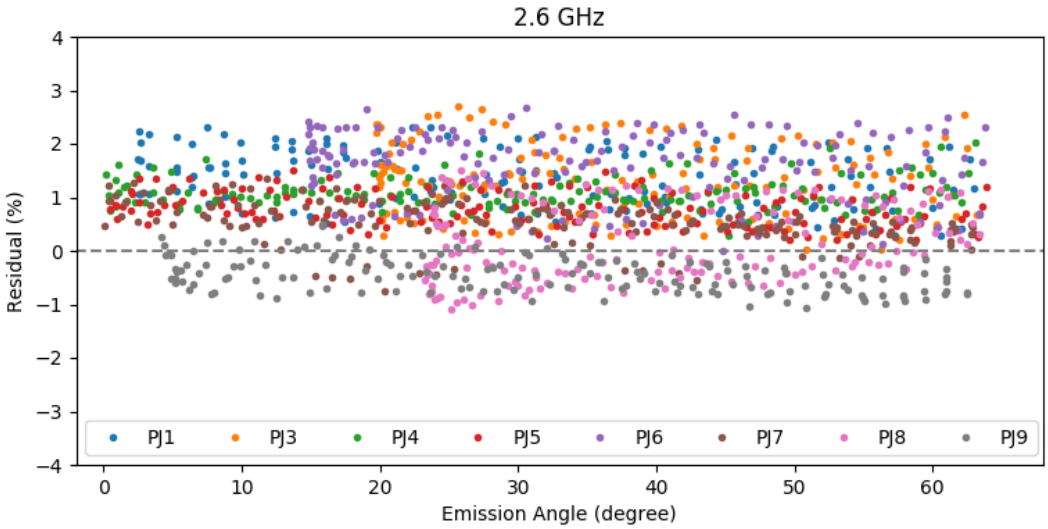

Figure B2. Residual antenna temperature as a function of emission angle. Each dot in the panel represents a single measurement made between 0 – 5 degrees north during PJ1-9.